Structure and magnetism of $Bi_2(Sr,Ca)_2MnO_{6+y}$ antiferromagnets with ferrimagnetic layers

W. R. McKinnon, E. Tselepis, Y. Le Page, S. P. McAlister, and G. Pleizier
Solid State Chemistry, Division of Chemistry, National Research Council of Canada, Ottawa, Canada K1A 0R9

J. M. Tarascon, P. F. Miceli, R. Ramesh, and G. W. Hull
Bell Communications Research, Red Bank, New Jersey 07701

J. V. Waszczak
AT&T Bell Laboratories, Murray Hill, New Jersey 07974

J. J. Rhyne and D. A. Neumann
National Institute of Standards and Technology, Gaithersburg, Maryland 20899
(Received 18 September 1989)

The layered oxides $Bi_2Sr_2MnO_{6+y}$ and $Bi_2Ca_2MnO_{6+y}$, the Mn analogs of the superconductor $Bi_2Sr_2CuO_{6+y}$, have anomalously sharp peaks in their magnetic susceptibility as a function of temperature at 120 and 100 K, respectively. We have studied the crystallographic and magnetic structure of these compounds by x-ray, electron, and neutron diffraction on both powders and single crystals and correlated the structure with the magnetic properties. In the magnetically ordered state, nearest-neighbor Mn moments are antiparallel and point normal to the MnO_2 layers. As in the superconducting Cu analog, the crystallographic structure of these compounds is distorted; because of the flexing of the atomic slabs associated with the distortion, not all the Mn in the crystal are crystallographically identical, so the magnetic moment of Mn can vary between these different lattice sites. As a result, the moments on adjacent sites do not exactly cancel, and each layer of MnO_2 is a ferrimagnet. A magnetic field can induce a transition from an antiferromagnetic phase, where the net moments of different layers are opposed, to a ferrimagnetic phase, where the net moments are aligned. A simple mean-field theory mimics the shape of the susceptibility versus temperature, and the deficiencies of the mean-field theory suggest the importance of fluctuations and domains.

I. INTRODUCTION

In the structure of the layered superconductors $Bi_2Sr_2Ca_{n-1}Cu_nO_y$, two types of packages of layers alternate along the c axis: n CuO_2 layers interleaved with Ca layers; and BiO bilayers sandwiched between SrO layers.[1] Superimposed on this substructure is a superstructure: a distortion that in the Cu compounds is incommensurate with the substructure. One goal in studying these materials is to explain how the superstructure affects other properties, especially superconductivity, but the incommensurability of the distortion has complicated this work because standard methods of crystallography cannot reveal fully the atomic displacements associated with the superstructure.[2]

Related compounds in which Cu is completely replaced by other transition metals M have similar structures, but in some cases the distortion is commensurate. This commensurability has allowed the full crystal structure, including the distortion, to be solved for two compounds, $Bi_2Sr_3Fe_2O_{9.2}$ (Ref. 3) and $Bi_2Ca_2CoO_{6+y}$.[4] The solution shows that the distortion originates in the Bi-O layers and is associated with extra oxygen inserted in these layers. This extra oxygen is undoubtedly also present in the cuprates, where it is presumably responsible for at least some of the doping that makes the cuprates metallic, although nonstoichiometry in the cations may also play a role.[5,6]

Like the structure, the magnetism of the cuprates is being studied for its possible links to superconductivity. Many of the cuprate superconductors have related "parent" compounds that are antiferromagnetic insulators. The magnetism should be influenced both by the layered nature of the structures and by any distortions. In orthorhombic La_2CuO_4, for example, the structure is distorted by rotations of the CuO_6 octahedra, and as a result the spins in the antiferromagnetic state cant slightly out of the CuO_2 planes.[7,8] The canting is responsible for the shape of the peak in the susceptibility near the transition,[9] and for the field-induced magnetic transition at lower temperatures.[7]

Related compounds in which Cu is replaced by other transition metals also show novel magnetic behavior. The compounds with $n=1$ and $M=$Co are antiferromagnets. Their magnetic susceptibilities as a function of temperature peak sharply, possibly indicating hidden ferromagnetism or canted spins.[10] This novel behavior is interesting in its own right, but studying the magnetism in these related compounds may also help us understand the magnetism, and so perhaps the superconductivity, in the cuprates.

To explore the relation between magnetism and struc-

ture in these layered compounds further, we prepared and studied Mn analogs of the Co compounds with $n=1$. The next section describes the techniques of sample preparation and measurement. Section III discusses our attempts to change the crystallographic distortion by doping the materials with Pb and La. Section IV presents the crystallographic structure. Sections V and VI describe the magnetization measurements and the magnetic structure, respectively, and Sec. VII compares these results with the predictions of a simple mean-field model. Section VIII compares the results with those for La_2CuO_4 and related compounds.

II. EXPERIMENTAL PROCEDURE

A. Sample preparation

Single crystals of $Bi_2Sr_2MnO_{6+y}$ and $Bi_2Ca_2MnO_{6+y}$ were prepared from powders of Bi_2O_3, $CaCO_3$ or $SrCO_3$, and MnO_2, mixed in the appropriate ratios. The powders were heated in an atmosphere of argon or nitrogen to 1300 °C over 8 h, held at this temperature for 1 h, cooled to 800 °C at 10 °C/h, then cooled to room temperature in 1 h. This procedure produced black lustrous crystals in the form of platelets, typically 3–5-mm long, 0.5–2-mm wide, and a few micrometers thick. In a second procedure, which produced smaller crystals of the Sr compound but did yield the crystal studied by x-ray diffraction, a stoichiometric mixture of the preceding compounds were heated in nitrogen to 1250 °C in 6 h, held for 2 h, cooled to 950 °C at 5 °C/h, then cooled to room temperature in 6 h.

Black-grey powders of single phase $Bi_2(Sr,Ca)_2MnO_{6+y}$ were prepared by reacting Bi_2O_3, $CaCO_3$ or $SrCO_3$, and MnO_2 at temperatures between 850 and 1050 °C in an atmosphere of argon or nitrogen. When these powders were heated in air, other oxides formed: yellow $BiO_{0.765}SrO_{0.235}O_{1.383}$ (Ref. 11) or yellow-green $Bi_6Ca_7O_{16}$ (Ref. 12), along with black-grey $SrMnO_{3-x}$ (Ref. 13) or $CaMnO_{3-x}$ (Ref. 14). Attempts to prepare $Bi_2Ba_2MnO_y$ failed. We usually obtained $BaMnO_{3-x}$ (green to black as x goes from 0 to 0.5) and a dark red phase that could be $Ba(Bi,Mn)O_x$ (since it has a similar x-ray pattern to $BaBiO_{2.77}$).

X-ray powder patterns of two samples made in air showed some peaks that might be due to $n=2$ phases (two layers of MnO_2 separated by Ca or Sr), but we have not isolated this phase. The $n=2$ phase is either hard to prepare, or else it does not exist. In either case, the $n=1$ phases of the Mn compounds are unlikely to be contaminated by intergrowths of the $n=2$ phase, in contrast to the analogous Co, Fe, or Cu compounds, where the $n=2$ phases form easily.

We tried to substitute Pb for Bi ($Bi_{2-x}Pb_xSr_2MnO_y$), or La for Sr ($Bi_2Sr_{2-x}La_xMnO_y$), hoping to modify the modulation of the structure. Mixtures of the starting materials already listed with appropriate amounts of PbO or La_2O_3 were reacted near 850 °C for several hours under nitrogen. We could not produce single-phase materials; the main phase was $Bi_2Sr_2MnO_{6+y}$. In the case of Pb, we did see shifts in the lattice parameters of the predominant phase. As we discuss in Sec. III, we believe these shifts to be from the formation of Sr deficient $Bi_2Sr_2MnO_{6+y}$; we confirmed this by making this Sr deficient material with the appropriate amount of Sr.

B. X-ray and electron diffraction

A single crystal of the Sr compound of size $0.34\times0.12\times0.07$ mm^3 was analyzed by single-crystal x-ray diffraction.[15] Like the Co analog $Bi_2Sr_2CoO_y$, it had the form of a rectangular platelet with its long side along b and its short side along c. The crystal structure was refined with standard least-squares methods using the NRCVAX system of programs.[16] Powders of both $Bi_2Sr_2MnO_{6+y}$ and $Bi_2Ca_2MnO_{6+y}$ were examined by transmission electron microscopy.

C. Magnetization measurements

Magnetization was measured on 2–17 mg of oriented single crystals (typically 3–10 crystals) in a SQUID magnetometer. These are dc measurements, and in what follows we define the mass susceptibility χ to be M/H, where M is the magnetization per unit mass and H the applied field. The crystals were in the form of platelets, typically 3–5-mm long by 1-mm wide, and at least 10 times thinner in the third direction. We assume that all crystals with the same aspect ratio are oriented in the same way as the crystal measured by x-ray diffraction. If this is not true, our attempts to find magnetic anisotropy in the a-b plane may have failed because the sample had mixtures of both a and b orientations in a given direction. The magnetization of one sample (10.5 mg) of randomly oriented crystals of $Bi_2Sr_2MnO_{6+y}$ sealed in a container under argon was also measured with a Faraday technique[17] to 1000 K.

D. Oxygen content

We could not find a technique to determine the oxygen content of these materials accurately. The materials did not fully dissolve in any acid we tried, making chemical methods impossible. The compounds appear to react with Pt containers in hydrogen, so thermogravimetic analysis (TGA) also failed. TGA measurements show that, under oxygen, the mass of samples prepared under nitrogen jumps by about 1% at 700 °C, and the sample decomposes into a mixture of the oxides found in Sec. II A. This decomposition explains why these samples cannot be preared in an oxygen atmosphere.

E. Resistance measurements

We measured the resistance of a crystal of $Bi_2Sr_2MnO_{6+y}$, 2.5×1.2 mm^2 in area and 22-μm thick, and for a crystal of $Bi_2Ca_2MnO_{6+y}$, 0.1×0.1 mm^2 in cross section and 0.55-mm long. Four leads were fixed on the Sr samples with silver paste, but only two on the Ca, sample, and a dc current of 0.5-μA current was used. The results showed that both compounds are semiconductors with a room-temperature resistivity of $1.1\times10^4\Omega$ cm and about $10^4\Omega$ cm for the Sr and Ca com-

pounds, respectively. The temperature dependence of resistivity approximately follows an Arrhenius law, with an activation energy of 0.16 eV and 0.12 eV, for Sr and Ca, respectively.

F. Neutron diffraction

Neutron diffraction was performed at the Neutron Beam Split-Core Reactor (NBSR) at the National Institute of Standards and Technology, on a triple-axis spectrometer set for zero-energy transfer. The incident energy was fixed at 14.7 meV and (002) highly oriented pyrolytic graphite was used for both monochromater and analyzer with collimators set at 40'-25'-25'-40'. Higher-order harmonics were eliminated using a pyrolytic graphite filter.

Powder samples of $Bi_2Sr_2MnO_{6+y}$ and $Bi_2Ca_2MnO_{6+y}$ were measured both above the ordering temperature and at 9 K. The data were subtracted (after correcting for thermal expansion) to obtain only the magnetic Bragg intensity. This subtraction was necessary due to the presence of various neighboring nuclear Bragg peaks arising from the superstructure. We also made some preliminary measurements on a single crystal of mass 8 mg.

III. CRYSTAL STRUCTURE

The atomic coordinates of $Bi_2Sr_2MnO_{6+y}$ determined in this work have already been reported.[18] This structure is body centered, isostructural with $Bi_2Sr_2CoO_{6+y}$.[4,18] The crystals of $Bi_2Ca_2MnO_y$ were thin, and did not grow flat enough to give good x-ray diffraction patterns, so we could not obtain their crystal structure. The lattice parameters of $Bi_2Sr_2MnO_{6+y}$ determined from least-squares refinements are $a=21.805(11)$ Å, $b=5.426(2)$ Å, $c=23.613(8)$ Å from single-crystal x-ray diffraction; those of $Bi_2Ca_2MnO_{6+y}$ are $a=21.374(2)$ Å, $b=5.360(1)$ Å, $c=23.151(2)$ Å from powder x-ray diffraction. (The numbers in parentheses are the estimated standard deviations in the last digit.)

TEM diffraction patterns in the (010) plane are shown for both $Bi_2Sr_2MnO_{6+y}$ and $Bi_2Ca_2MnO_{6+y}$ in Fig. 1. Both patterns show strong and weak bands of spots normal to a, a result of the modulation along a. The patterns are made up of two interpenetrating rectangular (almost square) subsets; the subset that contains the strongest spots corresponds to $(h+l)$ even, the other subset to $(h+l)$ odd. The weaker subset violates the body-centering condition. We have recently observed this weaker subset with x rays, and are planning to include it in the refinement of the structure.

This weaker subset of spots changes the symmetry relationships between different atomic layers, since they are no longer related by the operation of body centering. It is not expected, however, to change the structure of the individual MnO_2 layers significantly. In particular, it will not affect the aspect of the distortion most relevant to the magnetism. The distortion produces different types of Mn sites, each with similar, but not identical, environments. This differentiation of the Mn sites is the basis of the model proposed below to explain the magnetic results.

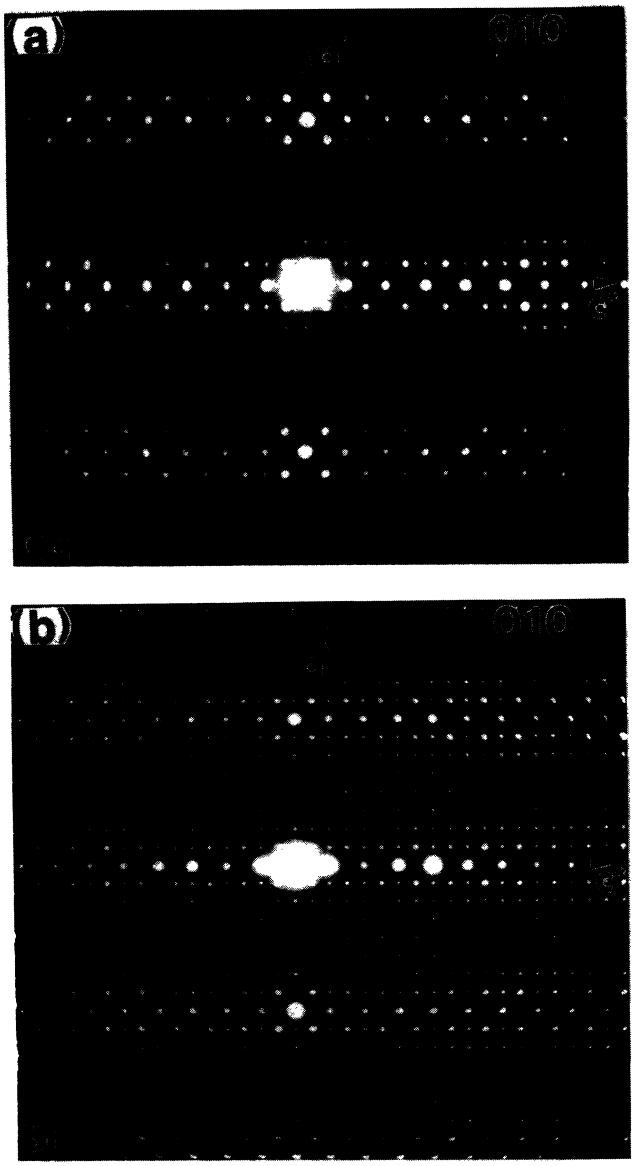

FIG. 1. Electron diffraction patterns for (a) $Bi_2Ca_2MnO_{6+y}$ and (b) $Bi_2Sr_2MnO_{6+y}$ in the (010) plane. Samples were taken from powders.

All Mn sites are surrounded by a distorted octahedron of oxygen, with the four oxygens in the MnO_2 layers closer than the two oxygens along c. The distances from Mn to the oxygens in the layers ranges from 1.90 to 1.96 Å, shorter than the distances expected for high-spin Mn^{2+}, but comparable to those of low-spin Mn^{2+} and high-spin and low-spin Mn^{3+}. Because of the uncertainties in the Mn-O distances of about 0.05 Å, we cannot infer the spin of the Mn atoms from the structure.

IV. NONSTOICHIOMETRY (Bi AND Sr) AND DOPING (Pb AND La)

Although our structure supports the idea that the distortion is associated with extra oxygen in the Bi-O layers,

other models of the distortion have been proposed, such as the ordering of Bi vacancies in the Bi-O layers,[19] or the ordering of Bi atoms in the Sr-O layers.[6] Proving which model is correct is difficult because the nonstoichiometry in the various components is hard to determine. One advantage of the Mn compounds over the Cu, Co, or Fe analogs is that they can be prepared only under nitrogen, so that the oxygen content is presumably well defined. We tried to vary some of the other stoichiometries in hopes of changing the wavelength of the distortion.

A. Sr and Bi nonstoichiometry

The lattice parameter of the dominant phase of powders of nominal composition $Bi_{2+x}Sr_2MnO_{6+y}$ and $Bi_2Sr_{2+z}MnO_{6+y}$ are given in Table I. In our refinements of the lattice parameters, c had the smallest fractional standard deviation and so is used to compare the various samples. The compounds listed in Table I are arranged in order of increasing c. The differences in the lattice parameters for the three samples of $Bi_2Sr_2MnO_{6+y}$ give an idea of the scatter in the experimental results. Within the error of our measurements, the c parameter did not change with excess Sr but decreased with excess Bi or a deficiency in Sr. This suggests the samples can accommodate either Sr vacancies or Bi on the Sr sites. Similar shifts in lattice parameters have been seen in $Bi_2Sr_2CuO_y$.[20]

TEM diffraction patterns show that the modulation in samples with Sr deficiency or excess Bi remains commensurate, with the same periodicity as in stoichiometric samples. This suggests that Sr vacancies or Bi in the Sr layer do not influence the structural modulation.

B. La and Pb substitution

The wavelength of the distortion in $Bi_2Sr_2CaCu_2O_y$ increases when Pb replaces Bi;[21] the increase is roughly that expected if the oxygen content of the (Bi,Pb)-O layers decreases to keep the total Cu valence constant.[18] We tried to change the modulation in the $n=1$ Mn compounds, both by substituting Pb for Bi and La for Sr. In both cases, the Pb or La did not go into the structure.

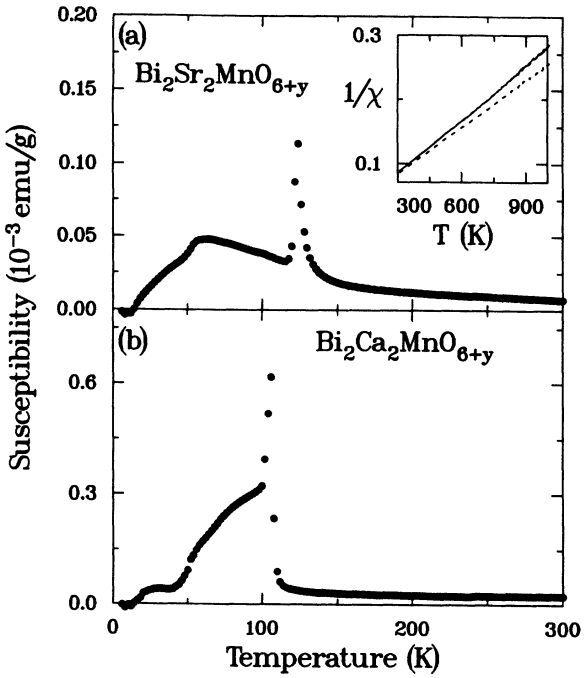

FIG. 2. Susceptibility vs temperature for (a) $Bi_2Sr_2MnO_{6+y}$ and (b) $Bi_2Ca_2MnO_{6+y}$ for warming in 500 G, after cooling in zero field. The inset to (a) shows the inverse susceptibility between 300 and 1000 K; the solid curve is the data, and the dashed curve is the data corrected for the diamagnetic background. The field is along c.

In the case of La, a second phase was observed, and the lattice parameters of the dominant $Bi_2Sr_2MnO_{6+y}$ phase did not change. For Pb, a second phase was also observed, but the lattice parameters of $Bi_2Sr_2MnO_{6+y}$ did change. The samples doped with Pb have a value of c smaller than 23.57 Å, undoped stoichiometric samples have c larger than 23.58 Å. Although at first glance this

TABLE I. Lattice parameters for $(Bi,Pb)_2Sr_2MnO_{6+y}$ and $Bi_2Sr_xMnO_{6+y}$, determined from powder x-ray diffraction by least-squares refinements. The a parameter is for the subcell (neglecting the crystallographic distortion). Standard deviations from the refinements are typically ±2 in the last digit. The compounds have been arranged in increasing c. The preparations were single phases except where noted.

Compound	a (Å)	b (Å)	c (Å)	Comments
$Bi_2Sr_{1.3}MnO_{6+y}$	5.454	5.440	23.543	Extra peaks
$Bi_2Sr_{1.8}MnO_{6+y}$	5.442	5.445	23.550	
$Bi_2Sr_{1.3}MnO_{6+y}$	5.452	5.442	23.558	Extra peaks
$Bi_2Sr_{1.8}Pb_{0.2}MnO_{6+y}$	5.435	5.430	23.562	
$Bi_2Sr_{1.8}MnO_{6+y}$	5.452	5.438	23.567	
$Bi_{1.5}Pb_{0.5}Sr_2MnO_{6+y}$	5.437	5.434	23.570	Extra peaks
$Bi_{2.3}Sr_2MnO_{6+y}$	5.450	5.440	23.581	
$Bi_2Sr_2MnO_{6+y}$	5.450	5.430	23.600	
$Bi_2Sr_{2.3}MnO_{6+y}$	5.420	5.430	23.607	Extra peaks
$Bi_2Sr_2MnO_{6+y}$	5.448	5.431	23.610	
$Bi_{1.8}Sr_2MnO_{6+y}$	5.445	5.439	23.618	
$Bi_2Sr_2MnO_{6+y}$	5.445	5.424	23.624	
$Bi_2Sr_{2.5}MnO_{6+y}$				Two phases

reduction in c suggests that Pb is entering the structure, we were unable to eliminate the second impurity phase. Moreover, as Table I shows, samples deficient in Sr or rich in Bi show a reduction in c similar to that for samples doped with Pb. We conclude that Pb does not enter the structure, but rather that it robs the structure of Sr producing either Sr vacancies or Bi in the Sr-O layers.

V. MAGNETIC PROPERTIES

Figure 2 shows the mass susceptibility χ (the measured magnetization divided by the field and the mass) versus temperature T for $Bi_2Sr_2MnO_{6+y}$ and $Bi_2Ca_2MnO_{6+y}$. The results in Fig. 2 were obtained on warming in 500 G, after the samples had been cooled in zero field; as discussed in the following, the susceptibility at low temperatures depends on field and on the previous history. For increasing T, χ for the Sr compound shows two maxima, a broad one near 50 K and a sharper one near 120 K. For the Ca compound, χ has an abrupt change of slope at 50 K and a sharp peak near 100 K.

The inset in Fig. 2(a) shows the inverse susceptibility in μemu/g for the Sr compound between 300 and 1000 K. The data to 900 K were fitted to a Curie-Weiss law plus a diamagnetic background; the dashed curve gives the data with the background removed. The background so determined was -0.39 μemu/g, compared to -1.11 μemu/g, calculated from the core diamagnetism of the various ions.[22] The other parameters in the fit were an effective (paramagnetic) moment of $n_p=4.96\mu_B$ and a Curie-Weiss temperature of $\Theta=-41$ K. This moment is close to that expected for high-spin Mn^{3+}, $n_p=4.90\mu_B$ (spin 2), but often the moment inferred from a Curie-Weiss law is smaller than the spin state of the ion would suggest, so the compound could also contain high-spin Mn^{2+} (spin 2.5, $n_p=5.92\mu_B$).

The effective moments determined by fitting the data on oriented single crystals below 300 K gave moments within 10% of the preceding fit but with a greater uncertainty because these temperatures are too close to the magnetic transition. Powders and single crystals of the Ca compound below 300 K gave $n_p=5.1\pm0.1\mu_B$ and $n_p=4.76\pm0.04\mu_B$, respectively, and both gave $\Theta=-40\pm5$ K, where the errors are the scatter from two or three different samples.

In both compounds, the magnetization differs from that in Fig. 2 if the history of thermal and magnetic treatment is different. To obtain Fig. 2(b), where the magnetization begins at zero at 10 K for the Ca compound, we had to null out the residual fields in the magnetometer, and we found that the curve in Fig. 2 changed appreciably if the field during cooling was changed by as little as 0.05 G. This history dependence is discussed in more detail in the following.

There are various ways to discuss the irreversibility at low temperatures. In spin glasses, for example, one distinguishes a thermal remanent magnetization (TRM) from an isothermal remanent magnetization (IRM).[23] The TRM is measured by cooling the sample in a field, then reducing the field to zero; the IRM by cooling a sample in zero field, then cycling the field up to some value and back to zero. Figure 3 shows the TRM for $Bi_2Sr_2MnO_{6+y}$ and $Bi_2Ca_2MnO_{6+y}$ at 10 K, as well as the magnetization $M(H_{cool})$ measured before the field is turned to zero; both are plotted as a function of the field during cooling (H_{cool}). There is a striking difference between the two compounds. In the Ca sample the TRM is almost the same as $M(H_{cool})$; the magnetization does not decrease significantly when the field is removed, suggesting ferromagnetism or ferrimagnetism. In the Sr sample the TRM is about five times smaller than $M(H_{cool})$, except below 2 kG [Fig. 3(b)], suggesting a field-induced transition. We consider further examples of the irreversibility as we discuss the Sr and Ca compounds in turn.

A. $Bi_2Sr_2MnO_{6+y}$

Figure 4(a) shows χ versus T for $Bi_2Sr_2MnO_{6+y}$ measured at 500 G, for increasing and decreasing T. When the sample is cooled in a field, the maximum at 50 K disappears; χ continues to increase as T decreases below 50 K. Figure 4 also shows $\chi(T)$ when a sample is cooled in zero field, warmed in a field to a temperature below 50 K, then cooled; χ stays constant on the second cooling. For fields applied normal to c, χ shows little evidence of this history dependence or of the sharp features [Fig. 4(b)]. In one sample, $M(T)$ increased by about 20% as

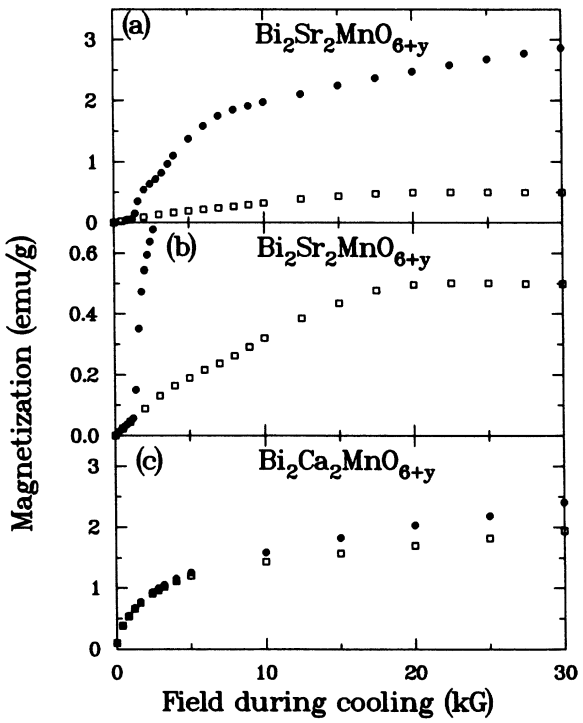

FIG. 3. Magnetization following cooling from 150 to 10 K, as a function of the field applied along c during the cooling. The sample was reheated to 150 K between each data point. The solid circles give the magnetization in the field at 10 K; the open squares the magnetization after the field is turned to zero, also at 10 K. (In spin glasses, the magnetization given by the open squares is called the thermal remanent magnetization, or TRM.) (a) and (b) show the same data for the $Bi_2Sr_2MnO_{6+y}$ on different vertical scales; (c) shows the data for $Bi_2Ca_2MnO_{6+y}$.

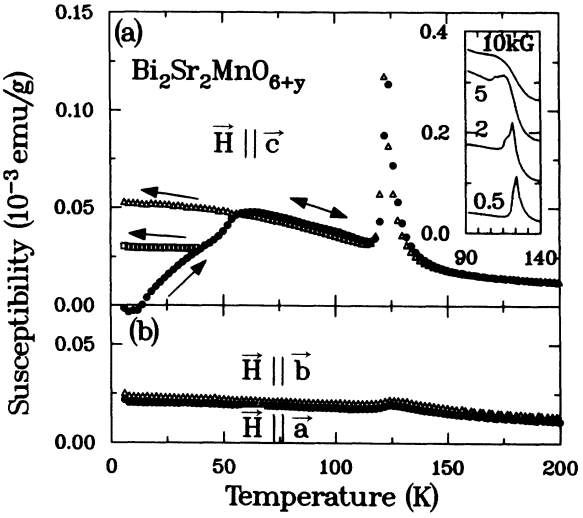

FIG. 4. Mass susceptibility (magnetization divided by field) per gram for $Bi_2Sr_2MnO_{6+y}$ for cooling and warming in 500 G. The curve for warming (solid circles) was measured after the sample was cooled in zero field; if the sample is cooled in 500 G, the data follows, to within experimental error, the data measured on cooling in 500 G (open triangles). Lying between these two curves at low temperatures is the susceptibility measured when a sample is cooled to 10 K in zero field, warmed to only 40 K in 500 G, then cooled in 500 G (open squares). The inset shows the shape of the peak near 120 K for different applied fields. The curves in the inset have been shifted upward for clarity. (b) Susceptibility vs temperature for warming in a field of 500 G for fields along *a* and *b*. In these directions, and for this sample, the warming and cooling curves are indistinguishable within experimental error.

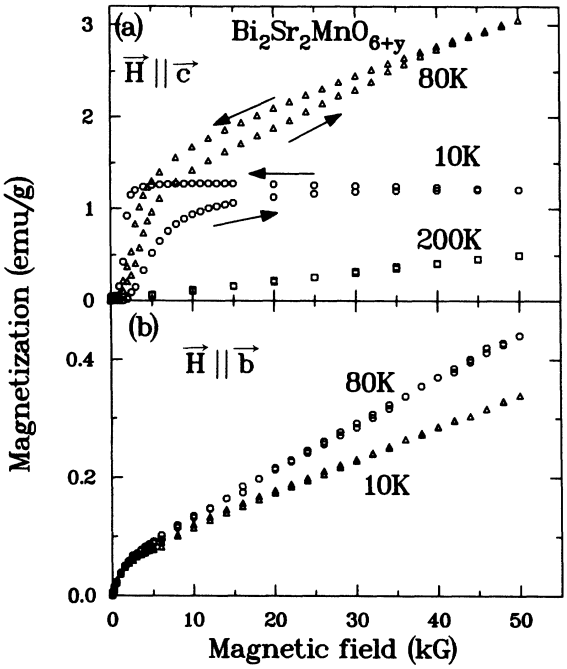

FIG. 5. Magnetization per unit mass of $Bi_2Sr_2MnO_{6+y}$ vs magnetic field at various temperatures, for (a) **H**||**c** and (b) **H**||**b**.

the sample cooled with **H**||**b**; in the sample shown in Fig. 4, the difference between cooling or warming was negligible.

The inset to Fig. 4(a) shows how the sharp peak in M disappears with increasing field. The rapid increases in M at 120 K persist, however, indicating that the boundary between the high-temperature paramagnetic state and the low-temperature state does not vary appreciably with field up to 50 kG.

Figure 5 shows the field dependence of M. For all temperatures below 120 K, M increases suddenly at some field below 5 kG as H increases. In some samples, $M(H)$ increased in two or three steps between 2 and 7 kG. For fields normal to c, M also increases rapidly, but only near zero field, as shown in Fig. 5(b). For fields over a few kG and temperatures below 120 K, M is about 10 times smaller for fields normal to c than for fields along c.

For H decreasing, $M(H)$ varies linearly with H above 10 kG. Figure 6 shows the slope and vertical intercept of that linear variation as a function of T, for H parallel to c and decreasing from a maximum value of 50 kG. The slope shows a maximum near 50 K, while the intercept shows no feature there; on the other hand, the intercept becomes negligible near 120 K, whereas the slope does not. The intercept measures the magnetization of the high-field phase; it decreases to zero at the phase transition to the paramagnetic state. The slope measures the differential susceptibility of the high-field phase, and decreases to zero at zero temperature.

Figure 6(b) shows the remanent magnetization as a sample is warmed, after it had been cooled in various

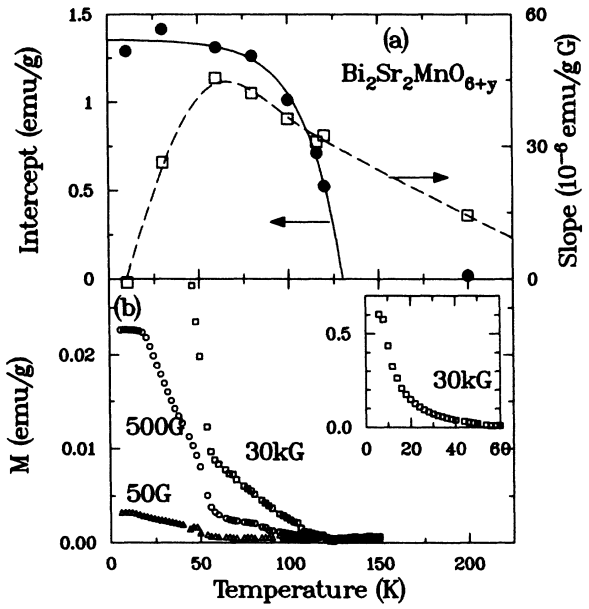

FIG. 6. (a) Intercept and slope of linear fits to data like those in Fig. 5, for the field parallel to c. The fits were to data measured as the field decreased from 50 to 10 kG. (b) Remanent magnetization (measured at zero field) after samples were cooled to 10 K in the fields indicated (fields parallel to c). The inset shows the data for 30 kG on a compressed scale.

fields. The remanent magnetization changes slope abruptly at 50 K, and is considerably smaller above 50 K than below. The maximum magnetization in the inset to Fig. 6(b), 0.6 emu/g, corresponds to a moment of $0.04\mu_B$ per Mn ion.

Although not obvious in Fig. 6, samples also show a small remanent magnetization after they have been cycled to high fields (an isothermal remanent magnetization, or IRM, in the terminology of spin glasses[23]). These IRM, 0.04 emu/g at 10 K and 0.02 emu/g at 80 K, are about 10 times smaller than the TRM shown in Fig. 6(a).

B. $Bi_2Ca_2MnO_{6+y}$

Although the curves in Fig. 2 suggest that the magnetism in the Ca compound is similar to that in the Sr one, the irreversible behavior at low temperatures is significantly different in the two compounds, as shown in Fig. 3. Both compounds show a similar magnetization in a field, but the Ca compound has a much larger magnetization than the Sr one in zero field after most histories of field and temperature. In fact, the Ca compound behaves like a classic ferromagnet at low temperatures. Figure 7 shows the magnetization as the field is cycled around a loop. This is behavior typical of the first cycle of a ferromagnet around a hysteresis loop. The saturation magnetization reached in Fig. 7 is about 0.7 emu/g, corresponding to a moment of $0.05\mu_B$ per Mn ion. The value of M at the beginning of the loop (in the center) depends sensitively on the field during cooling, as discussed in reference to Fig. 2.

Figure 8 compares M versus T for several cases. The curve showing warming in zero field after cooling in 500 G should be compared with the corresponding curve for the Sr compound in Fig. 6(b). That curve for the Ca compound shows a kink near 50 K, but the size of M is comparable below and above that temperature; in the Sr compound M is considerably smaller above 50 K than below 50 K. Near 100 K, the curves for the Ca compound depend on whether the temperature was being increased or decreased; in the Sr compound near 120 K, they are nearly identical. Finally, M obtained for fields normal to c for the Ca compound shows a large change as

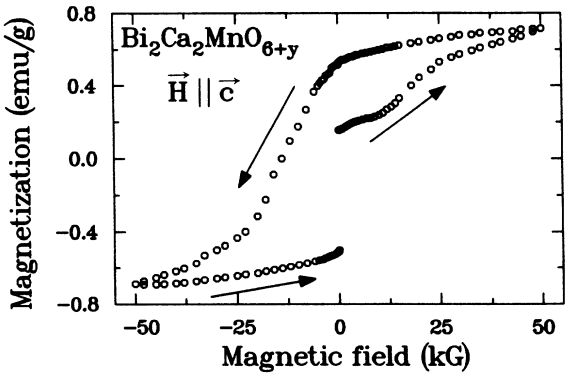

FIG. 7. Magnetization vs field for $Bi_2Ca_2MnO_{6+y}$, showing the first hystersis loop at 10 K. This should be compared to the data in Fig. 5 for $Bi_2Sr_2MnO_{6+y}$, which is half the loop and shows a much smaller remanence.

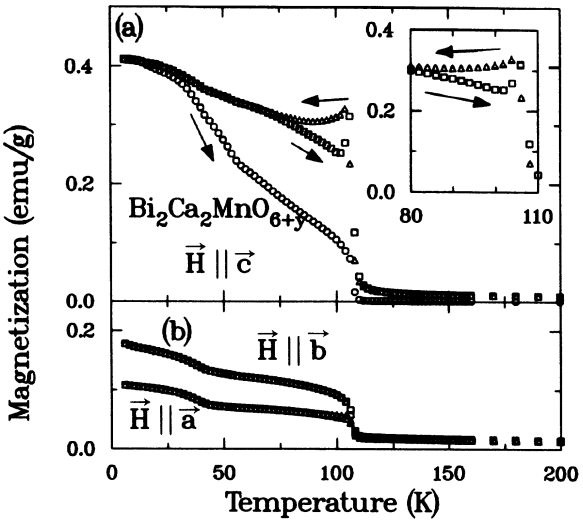

FIG. 8. Magnetization per gram for $Bi_2Ca_2MnO_{6+y}$ for cooling (triangles) and warming (squares) in 500 G, for fields (a) along c and (b) along a and b. Also shown in (a) are data obtained on warming in zero field after cooling in 500 G (circles). The data for warming and cooling in the field differ only near 100 K, and only for H||c; that region is expanded in the inset to (a).

T drops below 100 K; in the Sr compound there is little change at the corresponding temperature (120 K). The peaks in M are less obvious in Fig. 8(a) than in Fig. 2(b), where the sample was cooled in a field and measured on warming.

VI. NEUTRON DIFFRACTION

Figure 9 shows the magnetic neutron diffraction from powder samples of $Bi_2Sr_2MnO_{6+y}$ and $Bi_2Ca_2MnO_{6+y}$. The similarity between the two spectra indicates that the antiferromagnetic ordering in the two compounds is the same. To determine the spin arrangement in the crystal, we compared the measured intensities with those calculated for various cases. Because only antiferromagnetic reflections due to the subcell structure are observed, the superstructure could be safely ignored. Reasonable agreement between experiment and calculation was obtained only for moments directed along the c axis and the antiferromagnetic wave vector along [100] or [010]. The comparison is shown in Table II, for the [010] case, but the intensities calculated for [100] ordering are identical.

Because of the small difference between the a and b subcell lattice parameters, powder diffraction cannot distinguish between the [100] and [010] antiferromagnetic ordering directions. Consequently, we investigated a single crystal of $Bi_2Sr_2MnO_{6+y}$, and found only a (010) peak, with no measurable intensity at the (100) position in zero field. Thus, the antiferromagnetic ordering direction is along [010], perpendicular to the structural modulation along [100]. This result also implies that the 8-mg crystal used is a single domain both magnetically and crystallographically. The temperature dependence of the (010) reflection for this crystal is shown in the inset of Fig. 9(a).

Preliminary experiments on this crystal show that the (100) peak appears when a magnetic field is applied along the c axis, indicating that a weak ferromagnetic component must be associated with the [100]-type ordering.

The two possible antiferromagnetic orderings, [010] and [100], are illustrated in Fig. 10, where they are denoted AFM and FIM for reasons to be explained shortly.

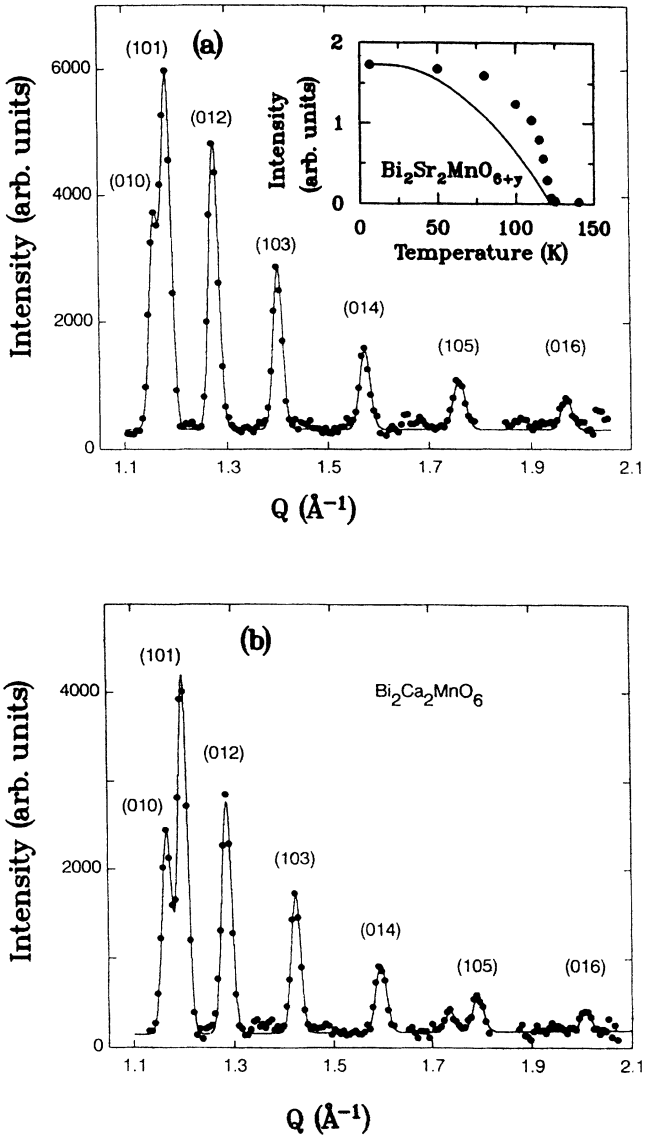

FIG. 9. Magnetic neutron powder diffraction for (a) $Bi_2Sr_2MnO_{6+y}$ and (b) $Bi_2Ca_2MnO_{6+y}$, obtained by subtracting data taken above the transition [200 K for (a) and 175 K for (b)] from data collected at 9 K. The solid curves are from least-squares fits of the peaks to a Gaussian line shape and were used in determining the integrated intensity. The inset of (a) shows the temperature dependence of the (010) reflection in zero field obtained from a single crystal. The solid curve in the inset is the square of a Brillouin function for spin 2, and is indistinguishable from the mean-field theory discussed in the text. The peaks are labeled assuming the antiferromagnetic ordering direction is along [010].

The figure is a projection of the Mn atoms along [010]; the bold circles represent atoms with positive fractional coordinates along [010], and the regular circles represent atoms with negative coordinates. In the subcell of $Bi_2Sr_2MnO_{6+y}$, the Mn ions form a face-centered orthorhombic (nearly tetragonal) lattice, and all the Mn sites are equivalent. The superstructure, a displacement wave along [100], produces three crystallographically different Mn sites, distinguished by symbols within the circles in the figure. The different Mn environments could produce slightly varying magnitudes or canting of the moments. This difference is represented in the figure by the difference in the length of the spins; for simplicity, the spins on one type of site are shown shorter than those on the other two types of site.

Because the displacement wave of the crystallographic distortion is along [100], a given (100) plane contains Mn sites of only one type, whereas a given (010) plane (the bold circles in the figure, for example) contain Mn sites of all types. Consequently, in antiferromagnetic ordering along [010] (the upper two layers of Mn ions in the figure) the moments must completely cancel, producing a true antiferromagnet (AFM). On the other hand, in ordering along [100] (the bottom two Mn layers in the figure), the moments may not completely cancel, leading to a ferrimagnetic (FIM) structure with a small net moment.

The in-plane Mn-Mn distance (normal to c) is only about $\frac{1}{3}$ the out-of-plane distance, so it is natural to view the Mn lattice as a stack of (001) Mn layers. In both the magnetic structures, the arrangement of a given layer is the same: adjacent Mn spins are antiparallel. Because of the differences in Mn environments, the moments of adja-

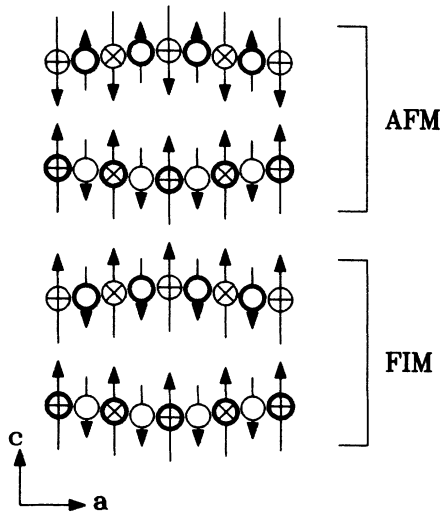

FIG. 10. Two possible magnetic structures consistent with the powder patterns in Fig. 9, projected along the b or [010] axis. The Mn positions are from the measured crystal structure; the distances along a and c are to scale, and the crystallographic distortion is not exaggerated. The three crystallographically distinct types of Mn sites are distinguished by open circles, circles enclosing +, and circles enclosing ×. The bold circles are atoms projected from positive positions along b; the regular circles are those projected from negative positions.

TABLE II. Relative intensities obtained from the data in Fig. 9 and compared to the calculated intensities assuming moments directed along the c axis and the antiferromagnetic ordering wave vector along the [010] direction. The (101) intensities are normalized to 100. The error on each of the measured relative intensities is ±2.

	Relative intensities		
Reflection	Measured $Bi_2Sr_2MnO_{6+y}$	Measured $Bi_2Ca_2MnO_{6+y}$	Calculated
(010)	58	60	55
(101)	100	100	100
(012)	84	66	73
(103)	46	37	47
(014)	25	21	28
(105)	18	12	16
(016)	9	6	9

cent spins are different, and each layer has a net moment. In the AFM structure, the net moments of adjacent layers cancel; in the FIM structure, they do not.

VII. MEAN-FIELD THEORY

The sharp peak in susceptibility at first glance suggests canting or hidden ferromagnetism.[10] However if canting were the explanation, the peak should be observed when the field is perpendicular to the direction that the spins take in the ordered state, not parallel to it. We propose that the shape of χ can be understood in terms of ferrimagnetism of the individual MnO_2 layers, and we present the mean-field solution of the simplest case that mimics the experimental results.

According to Néel's theory of ferrimagnetism,[24] $1/\chi$ versus T above the Curie temperature is a hyperbola. A plot of the Néel expression for χ (or of data for ferrimagnets, like those in Ref. 25) versus T resembles the results of Fig. 2 above the peak in χ. Below the transition, however, $\chi = M/H$ for a true ferrimagnet diverges as the system acquires a nonzero magnetization in zero field, whereas in Fig. 2 the anomaly in χ is finite. In short, χ looks like a ferrimagnet above the transition temperature, but like an antiferromagnet below. We suggest that this is precisely what it is: each layer of the compound is a ferrimagnet, but alternating layers couple antiferromagnetically, producing no net magnetization in the ordered state.

The Appendix outlines the calculation of the susceptibility for a simplified model that includes the essential features of the structure. Our goal was not to reproduce the experiment exactly, but rather to find the simplest model that captures the essential behavior. Based on Néel's theory of ferrimagnets, the model considers a body-centered tetragonal structure with two types of spins in each layer, with spins S_a and S_b, respectively, and identical g factors. In fact, the g factors probably differ, but this assumption reduces the number of parameters without significantly changing the results; the important thing is that the moments of the different types of sites are different.

We divide the tetragonal lattice into four sublattices, and consider the four interactions between spins on the various sublattices, as shown in Fig. 11. The numbering was chosen so that J_i is the interaction between spins on sublattice i with spins on sublattice 1. In this arrangement, we assume that the spin or moment of Mn sites of two of the three types of Mn sites in Fig. 10 are the same; this assumption should not change the qualitative details because in the observed magnetic structure the spins of those two types of sites are parallel in any given layer. The largest interaction is taken to be J_2, the nearest-neighbor interaction, which is assumed to be negative to account for the observed antiferromagnetic arrangement of spins in each layer. Because $S_a \neq S_b$, the antiferromagnetic arrangement gives each layer a net moment. If the net moments in all layers point in the same direction, the low-temperature phase is a ferrimagnet; if the net mo-

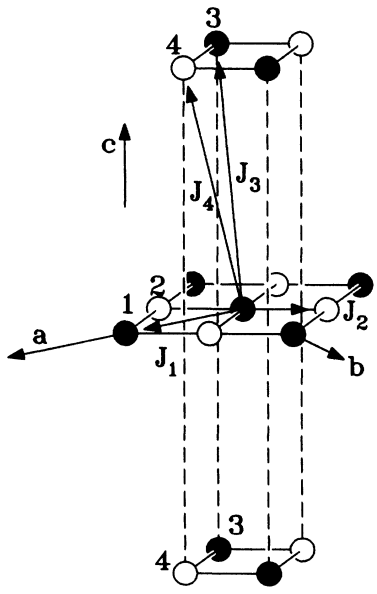

FIG. 11. The interactions and sublattices for the model considered in the text. Only the Mn atoms are shown. The open circles correspond to the open circles in Fig. 10, and the solid circles to the two other types of Mn atoms in Fig. 10. In a given a-b plane, the spins of open and solid circles point in opposite directions in the magnetically ordered state.

ments of adjacent layers point in opposite directions, it is an antiferromagnet, but one composed of ferrimagnetic layers.

The details of the mean-field analysis of the interactions in Fig. 11 are discussed in the Appendix. We now compare the calculations with experiment. The difference in the ordering or Néel temperature $T_N = 120$ K and the Curie-Weiss temperature $\Theta = -40$ K in $Bi_2Sr_2MnO_{6+y}$ can be accounted for if the second-neighbor interaction J_1 is positive (ferromagnetic) and half as large in magnitude as J_2. We used this relationship ($J_1 = -J_2/2$) as a constraint in comparing the calculations with the experiments. The susceptibility above the transition temperature, and the ordering temperature itself, can be found analytically; below the transition temperature, the mean-field equations can be solved by iteration.

The difference $S_a - S_b$ determines the width of the peak in $\chi(T)$: the larger the difference, the larger the width. Figure 12 shows two examples of the calculation, with this difference taken to be 0.64 and 0.10, and for comparison the data for $Bi_2Sr_2MnO_{6+y}$ on warming in 500 G after the compound was cooled in zero field. Although the larger difference in $S_a - S_b$ is needed to make the peak in the calculation as wide as the experiment, the difference is probably closer to the smaller value, for the following reasons. The model does not consider the two-dimensional fluctuations in the layers, and these fluctuations should broaden the peak beyond the mean-field result. Moreover, even in three-dimensional ferrimagnets, the susceptibility calculated in mean-field theory diverges much faster than experiment as the Curie temperature is approached from above, as shown, for example, in Ref. 25.

The MFT predicts that the saturation moment of the FIM phase should be $g\mu_B(S_a - S_b)/2$ per Mn atom at zero temperature. We can compare this with the magnetization reached by cooling in a field, in Fig. 3. If the solid circles in Fig. 3(a) and Fig. 3(c) are extrapolated to zero field, the magnetization is 1.62 emu/g and 1.23 emu/g for Sr and Ca, respectively. If we take $g = 2$ for all Mn atoms, this implies a difference in spin $S_a - S_b$ of 0.054 and 0.036, respectively. Preliminary experiments with neutron diffraction on $Bi_2Sr_2MnO_{6+y}$ suggest that the entire sample may not be fully in the FIM phase even at the highest fields in Fig. 3 (perhaps because of strains or inhomogeneities), so these numbers may underestimate $S_a - S_b$, but probably not more than a factor of 2. Thus the value $S_a - S_b$ of 0.10 in Fig. 12 is a reasonable estimate, certainly closer to the truth than 0.64.

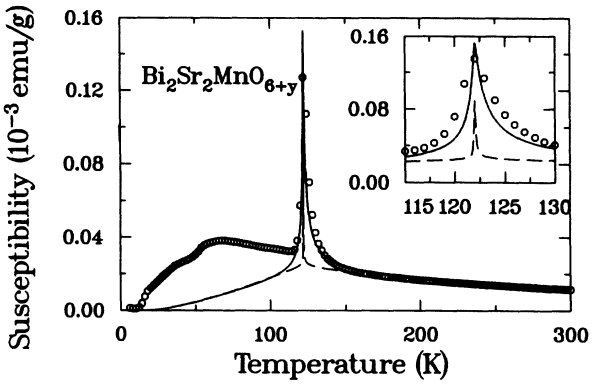

FIG. 12. Comparing the susceptibility of $Bi_2Sr_2MnO_{6+y}$ with the predictions of mean-field theory. The solid curve is for $S_a = 2.3$, $S_b = 1.659$, $T_s = 79.5$, $T_1 = -T_2/2$, $T_3 = T_4 = 6$ K. These parameters are unreasonable but were chosen to give a close fit to the data. The dashed curve is for $S_a = 2.05$, $S_b = 1.949$, $T_2 = 77.8$, $T_1 = -T_2/2$, $T_3 = T_4 = 0$, and show that the peak is too narrow when more reasonable parameters are used. In both cases, the value of S_b was chosen so that the high-temperature limit gives a Curie-Weiss law with an effective moment corresponding to a spin of 2.

The interactions normal to the MnO_2 planes, J_3 and J_4, determine the difference in the ordering temperatures of the AFM and FIM phase, and, in turn, the height of the peak in χ. The maximum of the wider MFT peak in Fig. 12 is too large unless J_3 and J_4 are assumed to be about 10% of J_2 in magnitude. Such values are orders of magnitude too large. In La_2CuO_4, for example, where the interlayer distance is half as large as in $Bi_2Sr_2MnO_{6+y}$, the out of plane interactions are about 10^{-4} times smaller than the nearest-neighbor in-plane ones.[9] This is another indication that the larger value of $S_a - S_b$ in Fig. 12 is unreasonable. On the other hand, for the smaller value of $S_a - S_b$, the height of the peak is set by the resolution of the calculation (the increment in temperature used was 0.1 K); the out-of-plane interactions for that curve in Fig. 12 were set to zero. In a real system with such a value of $S_a - S_b$ (if it were described by MFT), the peak height would probably be determined by inhomogeneities. Thus we cannot infer values of J_3 or J_4 from the shape of χ, at least in mean-field theory, for $S_a - S_b \doteq 0.1$.

Below the transition temperature, the MFT predicts that the system should switch discontinuously to the ferrimagnetic state at some field H_c. According to Eq. (2) of the Appendix, the energies of the AFM and FIM phases at zero temperature are equal at H_c given by

$$H_c = \frac{8J_3}{g\mu_B}(S_a - S_b) + \frac{16(J_4 - J_3)}{g\mu_B}\frac{S_a S_b}{S_a - S_b} .$$

If $S_a - S_b = 0.1$, $J_3 \approx J_4 \approx 10^{-4} J_2$, and the difference $J_3 - J_4 \approx 10^{-4} J_2$, then the first term in H_c is 3 G, and the second term is 2.5 kG. For comparison, the rapid increase in the magnetization at 10 K in Fig. 3(a) is at about 1.5 kG. Thus the difference in $J_3 - J_4$ determines H_c, for reasonable values of the out-of-plane interactions.

Experimentally, the magnetization does not increase discontinuously with field, whereas MFT predicts that it should. Moreover, MFT predicts that χ should decrease monotonically to zero at low temperatures in the AFM phase, again in contradiction to experiment. The hysteresis observed at low temperatures implies domains are present even at low fields. We suggest that a small amount of the FIM phase forms even in small fields, and that the susceptibility at low temperature is largely due to that FIM phase.

For $Bi_2Ca_2MnO_y$, which looks like a ferromagnet or a

ferrimagnet at low temperature, the sample is probably in the FIM phase, even in low fields. The interplane interactions in the MFT can be chosen so that the FIM phase is stable at all fields. In this case, the MFT predicts the usual magnetization for a ferrimagnet,[24] and does not predict a peak in $\chi = M/H$, in contradiction with Fig. 2 and Fig. 8. But the peak is large only when the sample is warmed after a special history that has made the measured magnetization small at low temperature, so that there are roughly equal numbers of up and down domains. When the sample is cooled in even a small field (presumably forming only domains of one direction), the peak is considerably smaller (Fig. 8). This peak may be explained by fluctuations. We conclude that $Bi_2Ca_2MnO_y$ has the FIM magnetic structure below 100 K at all fields, but this has not yet been confirmed by neutron diffraction.

VIII. DISCUSSION

The structural modulation in $Bi_2Sr_2MnO_y$ and $Bi_2Ca_2MnO_y$ strongly influences the magnetic properties in these compounds. Because of the modulation, not all the Mn in the crystal are crystallographically identical, so the magnetic moment of Mn can vary between these different lattice sites. As a result, each layer of MnO_2 can have a net moment below the transition. At low fields in $Bi_2Sr_2MnO_{6+y}$, the moments alternate from one layer to the next, leading to an antiferromagnetic phase. But an applied field can flip the moments, causing a field-induced transition. From the MFT discussed in the preceding section, we suggest that the ferrimagnetism of the individual layers is responsible for the sharp peak in the susceptibility in $Bi_2Sr_2MnO_{6+y}$.

But there are inconsistencies in the parameters in the MFT. If we calculate a value of $S_a - S_b$ from the magnetic moment of a sample cooled in a large field, then the peak in χ is too narrow; matching the peak in χ requires $S_a - S_b$ roughly 10 times larger, and also leads to unreasonable values for the out-of-plane interactions. A proper treatment of fluctuations may correct this problem.

We have assumed that the differences in S_a and S_b in the model are a result of differences in the size of the moment of Mn on crystallographically distinct sites. Another possibility is that these differences in moment are produced by canting. Because of the crystallographic distortion, the MnO_2 planes can be tilted locally by several degrees out of the $a-b$ plane. If the spin tries to lie normal to the local MnO_2 planes, it would tend to cant away from c. Perhaps the differences in S_a and S_b reflect differences in the component of spin along c, rather than differences in the total spin.

Whatever the role of canting, it is clear that the peak in χ in $Bi_2Sr_2MnO_{6+y}$ cannot have the same origin as the peak in La_2CuO_4 where canting has been shown to be important.[9] The spins in the ordered states of $Bi_2Sr_2MnO_{6+y}$ and $Bi_2Ca_2MnO_{6+y}$ point normal to the MnO_2 layers, whereas the spins in La_2MO_4, with $M = Cu$[7], Ni,[26] and Co,[27] lie in the MO_2 planes. In both families of compounds, the largest anomaly in χ is seen when the field is applied normal to the layers.[8,28] Thus the anomaly is produced by a field along the spins in $Bi_2Sr_2MnO_{6+y}$, and normal to them in La_2MO_4. Although the origins of the net moment of a given layer in La_2CuO_4 and $Bi_2Sr_2MnO_{6+y}$ are different, both compounds show field-induced transitions when the applied field aligns these net moments at some critical field.

The spins also point normal to layers of MnO_2 in Mn oxides with the K_2NiF_4 structure, in Ca_2MnO_4 (Ref. 29) and Sr_2MnO_4 (Ref. 30). These compounds show two-dimensional fluctuations; the susceptibility normal to the layers in Ca_2MnO_4 and Sr_2MnO_4 shows no anomalies at the ordering transition temperature (114 and 170 K, respectively), but does show a broad maximum at about 100 K above the transition. Thus the sharp peak in χ seen in $Bi_2Sr_2MnO_{6+y}$ is not seen in undistorted MnO_2 layers.

Oddly, the broad peak associated with two-dimensional fluctuations is not seen in $Bi_2Sr_2MnO_{6+y}$ up to 1000 K (Fig. 2), even though the MnO_2 layers are twice as far apart in $Bi_2Sr_2MnO_{6+y}$ as in Sr_2MnO_4, and one would therefore expect still weaker coupling. The MFT of Fig. 12 gives the nearest-neighbor in-plane interaction in $Bi_2Sr_2MnO_{6+y}$ J_2 to be $J_2/k = -5$ K. The corresponding values for Ca_2MnO_4 and Sr_2MnO_4 are -26 and -40 K; these were calculated from the two-dimensional Heisenberg model. Much of the disagreement between these values and ours arises because mean-field theory typically gives interactions less than half as large as those obtained from more accurate treatments. It is unlikely, therefore, that the peak expected from two-dimensional fluctuations could be pushed to temperatures above 1000 K in $Bi_2Sr_2MnO_{6+y}$ when it is near 300 K in Sr_2MnO_4.

In addition to its underestimation of the width of the peak in χ, the other major deficiency of the mean-field theory of Sec. VII is in its predictions at temperatures below T_N. The susceptibility of $Bi_2Sr_2MnO_{6+y}$ shows hysteresis even in the AFM or low-field state. To explain this second problem, we propose that small domains of the ferrimagnetic phase form even in small fields. In $Bi_2Ca_2MnO_{6+y}$, the FIM phase is probably the stable phase even at zero field. Another deficiency at low temperatures is that the intensity of the (010) peak in the inset to Fig. 9(a) is not described by MFT.

In spite of its limitations, though, the mean-field theory gives a plausible explanation of the relationships between the magnetization, magnetic structure, and the crystallographic distortion in $Bi_2Sr_2MnO_{6+y}$ and $Bi_2Ca_2MnO_{6+y}$. The discrepancies between theory and experiment may be resolved by more accurate theories that properly treat the two dimensionality of the MnO_2 layers.

Note added in proof. We have found that the temperatures we were using to prepare compounds with Bi replaced by Pb were too low. Powders of $Bi_{2-x}Pb_xSr_2MnO_{6+y}$ and $Bi_{2-x}Pb_xCa_2MnO_{6+y}$ can be prepared free of impurity phases at 960 °C in 48 h. For Sr, the solubility ranges of Pb are $0 < x < 0.6$ and $0.8 < x < 1.2$ at this temperature, according to powder x-ray diffraction.

APPENDIX: MEAN-FIELD THEORY

Consider a body-centered tetragonal lattice with two types of sites, a and b, in each layer. Figure 11 shows the four sublattices and the four interactions between sublattices. Although only nearest-neighbor interactions are shown, the interactions actually represent the total interaction between a spin on one sublattice and all the spins on another, in the spirit of mean-field theory. The interactions have been numbered so that J_i is the interaction between sublattice 1 and sublattice i. Spins S_1 and S_3 have maximum value S_a; S_2 and S_4 have maximum value S_b.

For convenience, we introduce a staggered field H_s that couples to $(S_1-S_2)-(S_3-S_4)$. The energy per cluster of four sites, E, is given by

$$\begin{aligned}E=&-g\mu_B H(S_1+S_2+S_3+S_4)\\&-g\mu_B H_s(S_1-S_2-S_3+S_4)\\&-4J_1(S_1^2+S_2^2+S_3^2+S_4^2)-8J_2(S_1S_2+S_3S_4)\\&-8J_3(S_1S_3+S_2S_4)-8J_4(S_1S_4+S_2S_3)\ .\end{aligned}\tag{1}$$

This expression assumes that both sites have the same g factor. Following Ref. 31, we drop the minus sign in the relation between spin and magnetic moment.

The dominant interaction is assumed to be J_2, which is antiferromagnetic (negative). This interaction drives the spins in the two sublattices in each layer to be antiparallel. But because S_a is different from S_b, there are two possible three-dimensional orderings consistent with negative J_2: a true antiferromagnet (AFM) in which the moment of one layer is opposed to that of the next, so the lattice has no net moment; and a ferrimagnet (FIM), in which the total moment of all layers is in the same direction, giving the lattice a net moment. At $T=0$, these ordered states are, for AFM and FIM,

$$S_1=S_a,S_2=-S_b,S_3=-S_a,S_4=S_b\ ,$$

$$S_1=S_a,S_2=-S_b,S_3=S_a,S_4=-S_b\ .$$

The difference in energy of these two states at $T=0$ and $H_s=0$ is

$$\begin{aligned}E_{\rm FIM}-E_{\rm AFM}=&-2g\mu_B H(S_a-S_b)\\&+32(J_3-J_4)S_aS_b-16J_3(S_a-S_b)^2\ .\end{aligned}\tag{2}$$

The first term on the right-hand side of Eq. (2) shows that an applied field favors the FIM state, as expected; in a field, the energy of the system is lower in the state with a net moment. The second and third terms show there are two different reasons that the AFM state could be favored over the FIM state in zero field: by a difference in the interactions between layers, J_3-J_4; and by a difference in the spin of the ion on each sublattice, S_a-S_b.

The spins $S_i, i=1,\ldots,4$ can be found in mean-field theory in the usual way,[31] from equations of the form

$$S_1=S_aB_{S_a}(x_1)\ ,\tag{3}$$

where B_{S_a} is the Brillouin function,[31] and x_1 is a dimensionless variable determined by the effective field on sublattice 1:

$$x_1=\frac{S_a}{kT}g\mu_B H_{\rm eff,1}\ .\tag{4}$$

The equations for the other sublattices are similar, except those for two and four involve S_b instead of S_a.

These equations can be linearized at small fields above the transition temperature, and then they separate into two pairs of equations. One pair involves the sums S_1+S_3 and S_2+S_4, and the other pair the differences S_1-S_3 and S_2-S_4. From these, the following quantities can be calculated:

$$\begin{aligned}S_\pm&=\frac{S_1\pm S_2\pm S_3+S_4}{4}\\&=\frac{g\mu_B H_\pm}{k}\frac{(1+\gamma)T+T_1\pm T_3-T_4\mp T_2}{T^2+2(1+\gamma)T(T_1\pm T_3)+(T_1\pm T_3)^2-(T_2\pm T_4)^2}\ ,\end{aligned}\tag{5}$$

where $H_+=H$, and $H_-=H_s$. The interactions J_i have been converted to temperatures with the relation

$$T_i=-\frac{8J_i}{3k}\sqrt{S_a(S_a+1)S_b(S_b+1)}\ .\tag{6}$$

The factor γ is one measure of the difference between S_a and S_b, and is defined by

$$\gamma=\frac{1}{2}\left[\left[\frac{S_a(S_a+1)}{S_b(S_b+1)}\right]^{1/4}-\left[\frac{S_b(S_b+1)}{S_a(S_a+1)}\right]^{1/4}\right]^2\ .\tag{7}$$

S_+ is the average spin per site, and so diverges at the transition temperature for any phase that has a net moment, and for the FIM phase in particular. The measured susceptibility is proportional to S_+. S_- is the staggered spin, or order parameter for the AFM phase.

For independent layers, ($T_3=T_4=0$) and equal sublattice spins ($S_a=S_b$, or $\gamma=0$), $S_\pm$ is given by

$$S_\pm=\frac{g\mu_B H_\pm}{k}\frac{1}{T\pm T_2+T_1}\ .\tag{8}$$

S_- diverges at the Néel temperature $T_N=T_2-T_1$. The Curie-Weiss temperature Θ is defined by

$$S_+=\frac{g\mu_B H_\pm}{k}\frac{1}{T-\Theta}\ ,\tag{9}$$

and so is given by $\Theta=-(T_2+T_1)$. The difference between $-\Theta$ and T_N is a special case of a more general result.[31] For $Bi_2Sr_2MnO_y$, where $T_N\approx 120$ K and $\Theta\approx -40$ K, we take $T_2\approx 80$ K and $T_1\approx -40$ K.

When the layers interact, or when S_a is not equal to S_b,

the transition temperatures for AFM and FIM phases are different. To lowest order, the difference is given by

$$T_{\mathrm{AFM}}-T_{\mathrm{FIM}}=2(T_3-T_4)+2\gamma T_3(T_2-T_1)/T_2 \ . \qquad (10)$$

Since the interactions T_3 and T_4 are expected to be orders of magnitude smaller than T_2, the difference in transition temperatures is small. If T_3 is positive, and larger than T_4, then the AFM phase has the higher transition temperature (S_- diverges at a higher temperature than S_+). Then the formation of the AFM phase interrupts the divergence in S_+. As the temperature decreases, the measured susceptibility (proportional to S_+) will begin to diverge, but will stop just short of its divergence, then decrease in the ordered AFM state, leading to a sharp peak as observed.

In comparing the MFT with experiment, we constrained the parameters. We chose S_a, then calculated S_b so that the high-temperature limit gives a Curie-Weiss moment appropriate for spin 2, as found experimentally (Fig. 2). We set $T_1=-T_2/2$ to account for the difference in T_N and $-\Theta$, then for given values of T_3 and T_4 we adjusted T_1 to give a transition temperature of 122 K. To calculate Fig. 12, we iterated the full (nonlinearized) equations for S_i. The iteration converged at all temperatures.

[1]J. M. Tarascon, W. R. McKinnon, P. Barboux, D. M. Hwang, B. G. Bagley, L. H. Greene, G. W. Hull, Y. Le Page, N. Stoffel, and M. Giroud, Phys. Rev. B **38**, 8885 (1988).

[2]Y. Gao, P. Lee, P. Coppens, M. A. Subramanian, and A. W. Sleight, Science **241**, 954 (1988).

[3]Y. Le Page, W. R. McKinnon, J.-M. Tarascon, and P. Barboux, Phys. Rev. B **40**, 6810 (1989).

[4]J. M. Tarascon, P. F. Miceli, P. Barboux, D. M. Hwang, G. W. Hull, M. Giroud, L. H. Greene, Y. Le Page, W. R. McKinnon, E. Tselepis, G. Pleizier, M. Eibschutz, D. A. Neumann, and J. J. Rhynes, Phys. Rev. B **39**, 11 587 (1989).

[5]Y. Gao, H. S. Sheu, V. Petricek, R. Restori, P. Coppens, A. Darovskikh, J. C. Phillips, A. W. Sleight, and M. A. Subramanian, Science **244**, 62 (1989).

[6]A. K. Cheetham, A. M. Chippendale, and S. J. Hibble, Nature **333**, 21 (1988).

[7]M. A. Kastner, R. J. Birgeneau, T. R. Thurston, P. J. Picone, H. P. Jennsen, D. R. Gabbe, M. Sato, K. Fukuda, S. Shamoto, Y. Endoh, D. Yamada, and G. Shirane, Phys. Rev. B **38**, 6636 (1988).

[8]S. W. Cheong, J. D. Thompson, and Z. Fisk, Phys. Rev. B **39**, 4395 (1989).

[9]T. Thio, T. R. Thurston, N. W. Preyer, P. J. Picone, M. A. Kastner, H. P. Jennsen, D. R. Gabbe, C. Y. Chen, R. J. Birgeneau, and A. Aharony, Phys. Rev. B **38**, 905 (1988).

[10]R. L. Carlin, *Magnetochemistry* (Springer, New York, 1986), p. 206.

[11]R. Guillermo, P. Conflant, J. C. Boivin, and D. Thomas, Rev. Chim. Miner. **15**, 153 (1978).

[12]P. Conflant, J. C. Boivin, and D. Thomas, J. Solid State Chem. **18**, 133 (1976).

[13]V. Caignaert, N. Nguyen, M. Hervieu, and B. Raveau, Mater. Res. Bull. **20**, 479 (1985).

[14]K. R. Poeppelmeier, M. E. Leonowicz, J. C. Scanlon, and J. M. Longo, J. Solid State Chem. **45**, 71 (1982).

[15]Y. Le Page, P. S. White, and E. J. Gabe, *Proceedings of the American Crystallography Association Meeting, Hamilton, 1986, Program Abstract Series 2* (ACA, New York, 1986), Vol. 14, p. 24.

[16]E. H. Gabe, A. C. Larson, F. L. Lee, and Y. Le Page, *Crystallographic Computing 3: Data Collection, Structure Determination, Proteins, and Databases,* edited by G. M. Sheldrick (Oxford University Press, New York, 1985), p. 167.

[17]F. J. DiSalvo and J. V. Waszczak, Phys. Rev. B **29**, 172 (1984).

[18]J. M. Tarascon, Y. Le Page, W. R. McKinnon, E. Tselepis, P. Barboux, B. G. Bagley, and R. Ramesh, in *High Temperature Superconductors: Relationships Between Properties, Structure, and Solid-State Chemistry,* edited by J. D. Jorgensen, K. Kitazawa, J. M. Tarascon, M. S. Thompson, and J. B. Torrance (Materials Research Society, Pittsburgh, 1989), p. 317.

[19]H. Maeda, Y. Tanaka, M. Fukutomi, T. Asano, K. Togano, H. Kumakura, M. Uehara, S. Ikeda, K. Ogawa, S. Horiushi, and Y. Matsui, Physica **153C**, 602 (1988).

[20]K. Kitazawa (unpublished).

[21]C. H. Chen, D. J. Werder, G. P. Espinosa, and A. S. Cooper, Phys. Rev. B **39**, 686 (1989).

[22]P. W. Selwood, *Magnetochemistry,* 2nd ed. (Interscience, New York, 1956), p. 78.

[23]For a review, see P. J. Ford, Contemp. Phys. **23**, 141 (1982).

[24]L. Neel, Ann. Phys. (Paris) **3**, 137 (1948).

[25]See, for example, R. Aleonard, J. Phys. Chem. Solids **15**, 167 (1960).

[26]G. Aeppli and D. J. Buttrey, Phys. Rev. Lett. **61**, 203 (1988).

[27]K. Yamada, M. Matsuda, Y. Endoh, B. Keimer, R. J. Birgeneau, S. Onodera, J. Mizusaki, T. Matsuura, and G. Shirane, Phys. Rev. B **39**, 2336 (1989).

[28]D. J. Buttrey, J. M. Honig, and C. N. R. Rao, J. Solid State Chem. **64**, 287 (1986).

[29]D. E. Cox, G. Shirane, R. J. Birgeneau, and J. B. MacChesney, Phys. Rev. **188**, 930 (1969).

[30]J.-C. Bouloux, J.-L. Soubeyroux, G. Le Flem, and P. Hagenmuller, J. Solid State Chem. **38**, 34 (1981).

[31]J. S. Smart, *Effective Field Theories of Magnetism* (Saunders, Philadelphia, 1966).

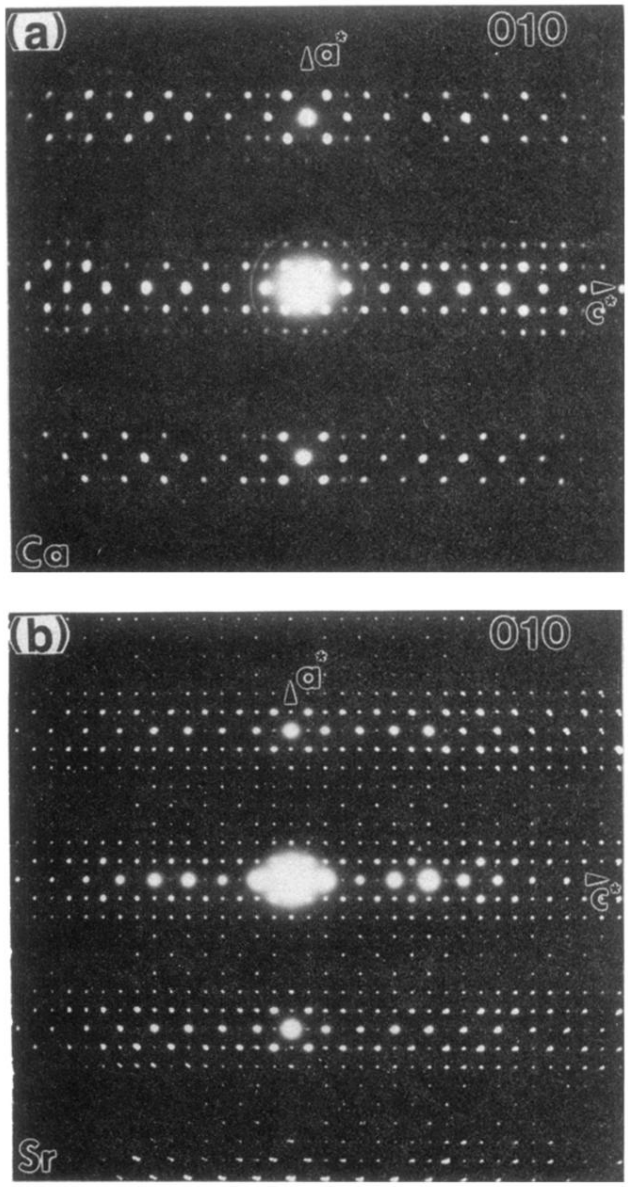

FIG. 1. Electron diffraction patterns for (a) $Bi_2Ca_2MnO_{6+y}$ and (b) $Bi_2Sr_2MnO_{6+y}$ in the (010) plane. Samples were taken from powders.